



# Predation without direction selectivity

Jenna Krizan<sup>a,b</sup>, Xiayingfang Song<sup>a,c</sup>, Michael J. Fitzpatrick<sup>a,b</sup> , Ning Shen<sup>a</sup> , Florentina Soto<sup>a</sup> , and Daniel Kerschensteiner<sup>a,d,e,1</sup>

Edited by Marla Feller, University of California, Berkeley, CA; received October 4, 2023; accepted January 27, 2024

Across the animal kingdom, visual predation relies on motion-sensing neurons in the superior colliculus (SC) and its orthologs. These neurons exhibit complex stimulus preferences, including direction selectivity, which is thought to be critical for tracking the unpredictable escape routes of prey. The source of direction selectivity in the SC is contested, and its contributions to predation have not been tested experimentally. Here, we use type-specific cell removal to show that narrow-field (NF) neurons in the mouse SC guide predation. *In vivo* recordings demonstrate that direction-selective responses of NF cells are independent of recently reported stimulus-edge effects. Monosynaptic retrograde tracing reveals that NF cells receive synaptic input from direction-selective ganglion cells. When we eliminate direction selectivity in the retina of adult mice, direction-selective responses in the SC, including in NF cells, are lost. However, eliminating retinal direction selectivity does not affect the hunting success or strategies of mice, even when direction selectivity is removed after mice have learned to hunt, and despite abolishing the gaze-stabilizing optokinetic reflex. Thus, our results identify the retinal source of direction selectivity in the SC. They show that NF cells in the SC guide predation, an essential spatial orienting task, independent of their direction selectivity, revealing behavioral multiplexing of complex neural feature preferences and highlighting the importance of feature-selective manipulations for neuroethology.

superior colliculus | retina | direction-selective | ganglion cells | narrow-field cells

Predation is a complex visual task essential to the survival of many animals (1). To succeed, predators need to detect camouflaged prey and track and capture them as they flee. Motion processing is central to all components of the task; it facilitates prey detection and guides pursuit and capture (2–6). In diverse species, predation is mediated by motion-sensitive neurons in the superior colliculus (SC) and its orthologs (e.g., the optic tectum in zebrafish and the lobula plate in arthropods) (7–13). Motion-sensitive neurons in the SC and its orthologs have complex stimulus preferences matching the conjunctions of visual features that initiate and maintain predatory pursuits (6, 7, 10, 13, 14). Many of these neurons are direction-selective (6–10, 13, 14). Direction selectivity is considered essential for predators to catch prey that frequently change course to escape. However, the contributions of direction selectivity to predation have not been tested experimentally.

Direction selectivity is restricted to specific neuron types in the mouse SC, including excitatory narrow-field (NF) cells (7, 14), which are thought to guide predation, and inhibitory Clbn4-positive neurons near the surface of the SC (15). A recent study raised concerns about prior work on direction selectivity in the SC, showing that direction-selective response can artificially be induced by stimulus edges (16). In addition, the origins of direction-selective responses in the SC are contested. Initial work indicated that the SC inherits direction selectivity from the retina (17) but relied on a manipulation subsequently found to disrupt the influence of retinal waves on SC circuit development (18). This latter work reported that direction selectivity in the SC is, at least in part, independent of the retina. All work on the origins of direction selectivity in the SC so far focused on the most superficial layers of the SC, restricting it to direction selectivity in the Clbn4-positive interneurons (15, 17, 18). Thus, the source of direction selectivity in the SC, particularly in NF cells, remains obscure.

Here, we show that NF cells guide predation and that direction-selective responses of NF cells are independent of stimulus edge effects. We explore the source of direction selectivity in the SC, including in NF cells, and determine its contributions to predation.

## Results

**Direction-Selective NF Cell Responses Are Independent of Stimulus Edge Effects.** NF cells can be genetically targeted in Grp-Cre mice (14). Using this targeting, two studies reported that many NF cells (~50%) respond strongly to stimuli moving in a preferred direction and weakly or not at all to motion in the opposite (i.e., null) direction (7, 14).

## Significance

Predators use vision to hunt. Processing motion, particularly changes in direction, is essential to detect, pursue, and capture prey. In many animals, the superior colliculus or equivalent visual midbrain structures mediate predation. Often, the neurons involved prefer motion in specific directions. The source of this direction selectivity and its importance to predation are unclear. Here, we show that narrow-field cells in the superior colliculus of mice guide predation. We find that these neurons inherit direction selectivity from a specific type of retinal ganglion cell (i.e., output neurons of the eye). Remarkably, eliminating direction selectivity in adult mice does not affect their hunting ability, revealing behavioral multiplexing of neurons with complex feature preferences.

Author affiliations: <sup>a</sup>Department of Ophthalmology and Visual Sciences, Washington University School of Medicine, St. Louis, MO 63110; <sup>b</sup>Graduate program in Neuroscience, Roy and Diana Vagelos Division of Biology and Biomedical Sciences, Washington University School of Medicine, St. Louis, MO 63110; <sup>c</sup>Graduate program in Biomedical Engineering, Department of Biomedical Engineering, Washington University in St. Louis, St. Louis, MO 63130; <sup>d</sup>Department of Neuroscience, Washington University School of Medicine, St. Louis, MO 63110; and <sup>e</sup>Department of Biomedical Engineering, Washington University in St. Louis, St. Louis, MO 63130

Author contributions: J.K. and D.K. designed research; J.K., X.S., M.J.F., N.S., and F.S. performed research; J.K., X.S., M.J.F., N.S., F.S., and D.K. analyzed data; and D.K. wrote the paper.

The authors declare no competing interest.

This article is a PNAS Direct Submission.

Copyright © 2024 the Author(s). Published by PNAS. This article is distributed under [Creative Commons Attribution-NonCommercial-NoDerivatives License 4.0 \(CC BY-NC-ND\)](#).

<sup>1</sup>To whom correspondence may be addressed. Email: kerschensteiner@wustl.edu.

This article contains supporting information online at <https://www.pnas.org/lookup/suppl/doi:10.1073/pnas.231721821/-DCSupplemental>.

Published March 14, 2024.

In addition to a propensity for direction-selective responses, NF cells tend to have smaller receptive fields ( $<300 \text{ deg}^2$ ) than other SC neurons (7, 14). We recorded the activity of SC neurons on multielectrode silicon probes in awake head-fixed mice that were free to run on a cylindrical treadmill in an immersive stimulation dome, encompassing 180 deg and 120 deg of the mouse's visual field in azimuth and elevation, respectively (Fig. 1A,  $n = 332$  neurons recorded in 12 mice). Because locomotion has only minor effects on visual responses in the SC (and none on direction selectivity), we did not consider it further in our analyses (19, 20).

A recent study raised concerns about prior work on direction and orientation selectivity in the SC, demonstrating that stimulus edges can artificially induce orientation and direction tuning (16). To avoid this confound, we presented motion in a drifting grid of dots covering the immersive stimulation dome (21). We used sparse noise stimuli to map the ON and OFF receptive fields of SC neurons and restricted our analyses of motion responses to neurons with receptive fields  $>20 \text{ deg}$  from the stimulus edge. We found that direction-selective cells had smaller receptive fields than non-direction-selective cells (Fig. 1B and C), consistent with an enrichment of NF cells in the direction-selective population. We conservatively identified NF cells as direction-selective neurons with receptive fields  $<300 \text{ deg}^2$  (Fig. 1D). These putative NF cells were similar in their speed tuning to non-NF cells (Fig. 1E) but showed more balanced ON and OFF receptive fields (Fig. 1F).

This division, which was not part of the classification process, suggests that our identification of NF cells preferentially selected a specific neuron type. Recent single-nuclei RNA sequencing suggests that NF cells may comprise molecularly distinct subtypes (15). Whether direction-selective and non-direction-selective NF cells align with different molecular subtypes is unclear. Nonetheless, our recordings show that direction-selective responses among NF cells are independent of stimulus edge effects.

**NF Cells Guide Predation.** To evaluate the contributions of NF cells (direction-selective and non-direction-selective) to predation, we injected AAVs Cre-dependently expressing Caspase 3 bilaterally into the SCs of Grp-Cre mice (i.e., NF-Casp3), inducing cell type-specific apoptosis (22); we injected Grp-Cre mice with AAVs Cre-dependently expressing jGCaMP6s (23) as controls. We waited for at least 4 wk postinjection before testing the ability of mice to hunt crickets. NF-Casp3 mice took, on average, more than five times as long to catch crickets than control littermates (Fig. 1 G–I). They exhibited deficits in all phases of the behavior: prey detection (measured by the interval between approaches, Fig. 1 J and K), pursuit (measured by the probability of converting approaches into contacts, Fig. 1 L and M), and capture (measured by the probability of converting contacts into captures, Fig. 1 N and O). Together with previous work (7), our results thus demonstrate that NF cells in the SC are critical for visual predation in mice.

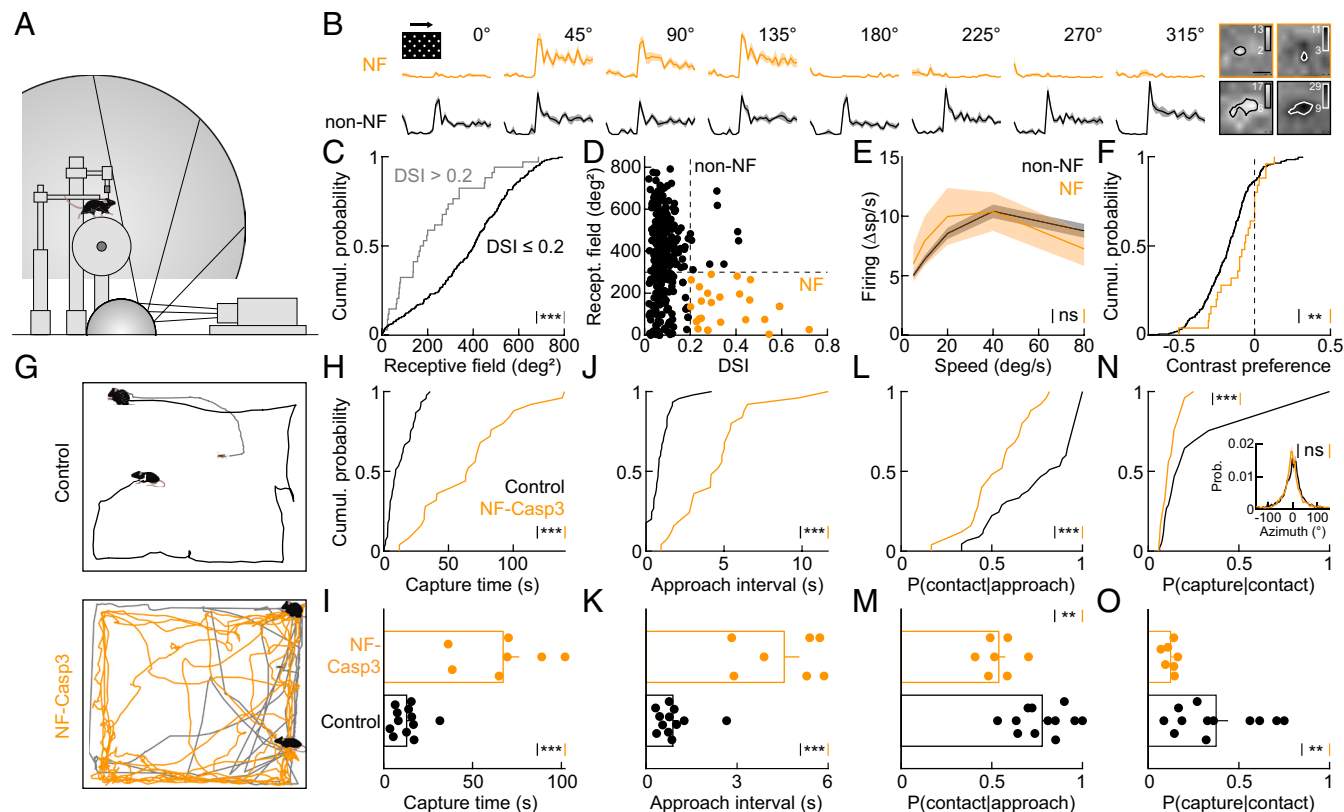


**Fig. 1.** Direction-selective NF cells in the mouse SC guide predation. (A) Schematic of the *in vivo* multielectrode recording setup, in which mice are head-fixed and free to run on a cylindrical treadmill in the center of an immersive dome on which visual stimuli are presented from a digital light projector via a curved mirror. (B) Example responses of a putative NF cell (i.e., receptive field  $< 300 \text{ deg}^2$ , DSI  $> 0.2$ ) and a neighboring neuron to a drifting spot grid stimulus. ON and OFF receptive fields mapped by sparse noise stimuli are shown on the right. (C) Cumulative distribution of the receptive field sizes for direction-selective (DSI  $> 0.2$ ,  $n = 34$  cells, 12 mice) and non-direction-selective (DSI  $\leq 0.2$ ,  $n = 298$  cells). (D) Scatter plot of SC neurons receptive field size and DSI. Putative NF cells are highlighted in orange ( $n = 25$  cells). (E) Tuning curve (mean, SEM) of NF (orange) and non-NF cell (black,  $n = 307$  cells) responses to drifting grid stimuli moving at different speeds in their preferred directions. (F) Cumulative probability of the contrast preference index (negative = OFF preference, positive = ON preference) of NF and non-NF cells. (G) Traces of representative hunting trials of control (black) and NF-Casp3 mice (orange). (H and I) Summary data comparing capture times of control and NF-Casp3 mice across all trials (H, control  $n = 45$  trials, NF-Casp3  $n = 25$  trials) or after the three to four trials of each mouse (I, control  $n = 12$  mice, NF-Casp3  $n = 7$  mice). (J and K) analogous to (H and I) for approach intervals. (L and M) analogous to (H and I) for the probability of converting approaches into contacts. (N and O) analogous to (H and I) for the probability of converting contacts into captures. The inset in N shows the distribution of the cricket in azimuth within the head-centric visual field of mice during approach and contact. Throughout this figure, ns indicates  $P > 0.05$ , \*\* $P < 0.01$ , and \*\*\* $P < 0.001$ .

**NF Cells Receive Input from ON-OFF Direction-Selective Ganglion Cells (ooDSGCs).** NF cells project from the superficial to deeper layers of the SC and the parabigeminal nucleus (PBGN) (14). Retrograde tracing of retinal inputs to SC neurons innervating the PBGN showed that ooDSGCs contribute to this pathway (24). However, NF cells are not the only SC neurons innervating the PBGN (14). To examine the ganglion cell input to NF cells and estimate the fraction provided by ooDSGCs, we performed retrograde monosynaptic rabies tracing experiments (25, 26). We first injected the SC of Grp-Cre mice with a Cre-dependent helper AAV and then, 3 to 4 wk later, with an EnVA-pseudotyped G-deleted rabies virus (Fig. 2A). The rabies virus requires expression of the EnVA-receptor TVA from the helper AAV to infect the target cell and an optimized G glycoprotein to jump one synapse upstream (25, 26). We analyzed ganglion cell labeling in the retina five to seven days after rabies virus injections. Staining for the ooDSGC-specific marker cocaine- and amphetamine-regulated transcript (CART) (27) indicated that  $15.8 \pm 0.9\%$  ( $n = 5$  mice) of NF cell ganglion cell partners are ooDSGCs. Consistent with this finding, in sparsely labeled regions of the retina, we frequently observed ganglion cells with bistratified dendrite arbors overlapping the ChAT-bands (i.e., costratifying with starburst amacrine cells, Fig. 2D). When we targeted these cells for patch-clamp recordings under two-photon guidance, they exhibited direction-selective responses to drifting grating stimuli (Fig. 2E). Together, these results demonstrate that ooDSGCs innervate NF cells in the SC, accounting for ~16% of their ganglion cell input. Whether this input distributes unevenly between direction-selective and non-direction-selective NF cells remains to be explored.

**SC Neurons, Including NF Cells, Inherit Direction Selectivity from the Retina.** We next wanted to test whether the direction-selective responses of NF cells and other SC neurons depend on direction-selective signals from the retina. To avoid the confounds of previous developmental manipulations (17, 18), we abolished retinal direction selectivity by removing starburst amacrine cells from mature circuits with binocular diphtheria toxin injections in 2- to 3-mo-old SAC-DTR mice (28). Two weeks after the injections, most starburst amacrine cells were gone without disrupting the overall retinal anatomy or loss of photoreceptors (Fig. 3A–C). We crossed SAC-DTR to DRD4-EGFP mice to fluorescently label ooDSGCs (27, 29, 30). Targeting fluorescent ooDSGCs under

two-photon guidance for patch-clamp recordings showed that their direction preferences were eliminated in SAC-DTR but not in control mice injected with diphtheria toxin (Fig. 3D and E).

To test how the loss of retinal direction selectivity affected responses in the SC, we performed *in vivo* multielectrode recordings in awake head-fixed SAC-DTR and control mice (Fig. 3F). To enrich for NF cells, we first restricted our analysis to neurons with receptive fields  $<300$  deg $^2$  (7, 14). Whereas in control mice, 20.3% of these neurons were direction-selective (i.e., DSI > 0.2), only 2.4% passed the DSI threshold in SAC-DTR mice (Fig. 3G). This finding held when we included all SC neurons in our analysis (DSI > 0.2; control: 10.2%, SAC-DTR: 1.7%, *SI Appendix*, Fig. S1). The loss of direction selectivity in small-receptive-field SC neurons occurred without changes in their speed preference (i.e., preferring fast over slow motion, Fig. 3H). It was accompanied by a slight shift in contrast preferences toward more balance between ON and OFF responses (Fig. 3I). Orientation selectivity was unchanged in SAC-DTR compared to control mice (Fig. 3J), indicating that it does not arise from the convergence of ooDSGCs with opposite motion preferences, a mechanism suggested for orientation-selective dLGN neurons (31, 32). In conjunction with the retrograde tracing experiments (Fig. 2), our recordings thus demonstrate that SC neurons, including NF cells, inherit their direction selectivity from ooDSGCs.

**Predation without Direction Selectivity.** The ability to eliminate direction selectivity without eliminating NF cells or silencing their responses allowed us to test the behavioral importance of the conserved visual feature preference of predation-mediated neurons in the SC and its orthologs (6–10, 14). We injected two- to three-month-old SAC-DTR and control mice binocularly with diphtheria toxin. Two weeks after the injections, we food-deprived the mice, acclimated them to the behavioral arena, and allowed them to hunt crickets for 5 d before testing their performance (33, 34). Remarkably, abolishing direction selectivity had no discernible impact on predation (Fig. 4A). SAC-DTR mice caught crickets as quickly as control littermates (Fig. 4B and C) and showed no deficits in detecting (Fig. 4D and E), pursuing (Fig. 4F and G), or capturing their prey (Fig. 4H and I).

Mapping the contributions of retinal direction selectivity across visual behaviors confirmed that it is critical for the gaze-stabilizing optokinetic reflex (Fig. 4J) (35, 36) and showed that it does not

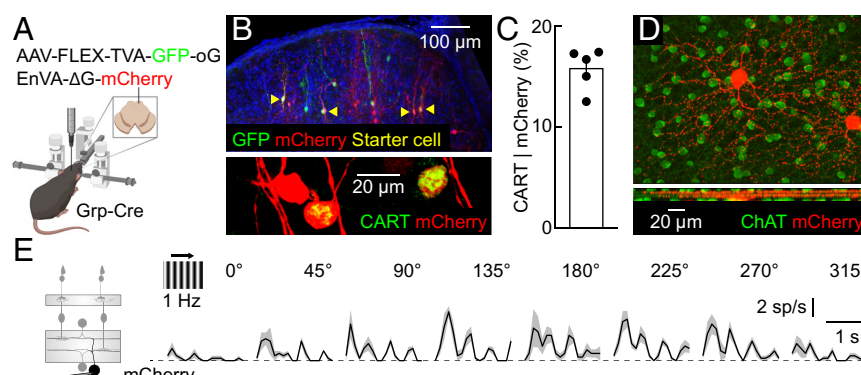


**Fig. 2.** NF cells in the SC receive input from ooDSGCs. (A) Schematic illustrating stereotaxic injections for monosynaptic retrograde rabies virus tracing strategy. A helper AAV (AAV-FLEX-TVA-GFP-oG) was injected into the SC of Grp-Cre mice. Three to four weeks later, a pseudotyped G-deleted rabies virus was injected at the same coordinates. (B) Top: Representative image of a section through the SC showing helper AAV expression (green) and rabies virus expression (red). Colabeled cells are starter cells for monosynaptic retrograde tracing. Bottom: Representative image of a retinal flat mount, showing cells infected by rabies virus (red) and immunohistochemistry for CART (green), a cell type-specific marker of ooDSGCs. (C) Summary data for the fraction of retrogradely labeled ganglion cells that were positive for CART ( $n = 5$  mice). (D) Representative orthogonal projections of a confocal image stack of a retrogradely labeled ooDSGC, whose dendrites costratify with ChAT-stained starburst amacrine cell dendrites. (E) Representative spike rate responses of retrogradely labeled ganglion cells with bistratified dendrites (i.e., putative ooDSGCs) to a drifting sine-wave grating.

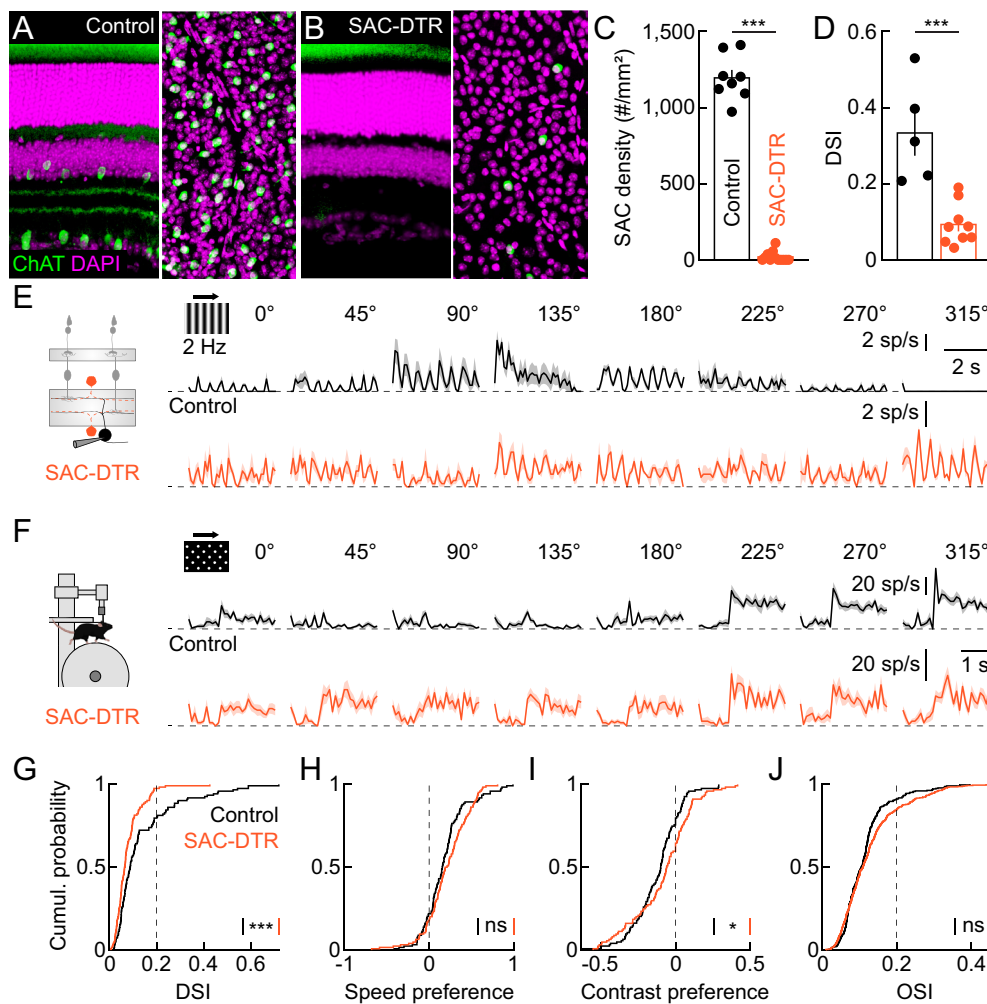


**Fig. 3.** SC neurons inherit direction selectivity from the retina. (*A* and *B*) Representative images of vibratome slices (*Left*) and flat mount views of the inner nuclear layer (*Right*) in control (*A*) and SAC-DTR mice (*B*) injected with diphtheria toxin. (*C*) Summary data of the starburst amacrine cell density in the inner nuclear layer of control (black,  $n = 8$  mice) and SAC-DTR mice (orange,  $n = 12$  mice) injected with diphtheria toxin. (*D* and *E*) Representative traces (*E*) and summary data (*D*) of the DSI of oodSGCs transgenically labeled by Drd4-EGFP in control ( $n = 5$  cells) and SAC-DTR ( $n = 9$  cells) mice injected with diphtheria toxin. (*F*) Representative spike response traces of small-receptive-field cells in the SC of control (black) and SAC-DTR mice (orange) injected with diphtheria toxin to spot grid stimuli drifting in different directions. (*G*) Cumulative probability of the DSIs of small-receptive-field neurons in control ( $n = 123$  cells, 12 mice) and SAC-DTR mice ( $n = 124$  cells, 18 mice) injected with diphtheria toxin. (*H* and *I*) Cumulative distributions comparing speed preference (*H*) and contrast preference indices (*I*) of small-receptive-field neurons in control and SAC-DTR mice injected with diphtheria toxin. (*J*) Cumulative distribution of OSIs across all neurons in the SC recorded in control ( $n = 332$  cells) and SAC-DTR mice ( $n = 473$  cells) injected with diphtheria toxin. Throughout this figure, ns indicates  $P > 0.05$ , \* $P < 0.05$ , and \*\*\* $P < 0.001$ .

influence the pupillary light response (Fig. 4*K*) or depth perception (Fig. 4*L*).

In the abovementioned experiments, starburst amacrine cells were eliminated before mice were introduced to crickets and learned to hunt them. Thus, we wondered whether, without starburst amacrine cells, mice adopt alternative strategies for predation that obscure the regular contributions of direction selectivity. We, therefore, analyzed the time course of starburst amacrine cell removal and optokinetic reflex responses after binocular diphtheria toxin injections (day 0) in SAC-DTR and control mice. Starburst amacrine cell numbers in the inner nuclear (i.e., OFF SACs) and ganglion cell layers (i.e., ON SACs) were relatively stable until 9 d after the injections, when they dropped precipitously (Fig. 5 *A* and *B*). Ten days after the injections, nearly all starburst amacrine cells were gone (Fig. 5 *A* and *B*). Similarly, the optokinetic reflex was maintained until 8 or 9 d after the injections but abolished by day ten (Fig. 5 *C* and *D*). The temporal precision of starburst ablation and behavioral deficits allowed us to test the contributions of direction selectivity to predation acutely.

We food-deprived mice, acclimated them to the behavioral arena and allowed them to hunt crickets for five days, starting four

days after binocular diphtheria toxin injections. During this period, direction selectivity should be largely intact. We tested the hunting performance of SAC-DTR and control mice the next day (i.e., 10 d after the injections) when direction selectivity should be eliminated. The acute elimination of direction selectivity caused no deficits in the predation of mice that had learned to hunt with intact direction selectivity (Fig. 5 *E*). The overall capture times (Fig. 5 *F* and *G*), approach intervals (i.e., prey detection, Fig. 5 *H* and *I*), and success of converting approaches into contacts (i.e., prey pursuit, Fig. 5 *J* and *K*) and contacts into captures (i.e., prey capture, Fig. 5 *L* and *M*) were not significantly different between SAC-DTR and control mice. Finally, irrespective of whether we removed starburst amacrine cells before or after mice learned to hunt, mice kept crickets in their binocular visual fields during approach and contact (Figs. 4*H* and 5*L*), indicating that prey tracking is independent of direction selectivity and confirming that hunting remains visually guided in SAC-DTR mice (33).

Retinal direction selectivity is critical for gaze-stabilizing eye movements mediated by the accessory optic system (Fig. 4*J*) (35, 36), which could regulate predation independent of the SC. To test this, we pharmacogenetically silenced the nuclei of the accessory optic

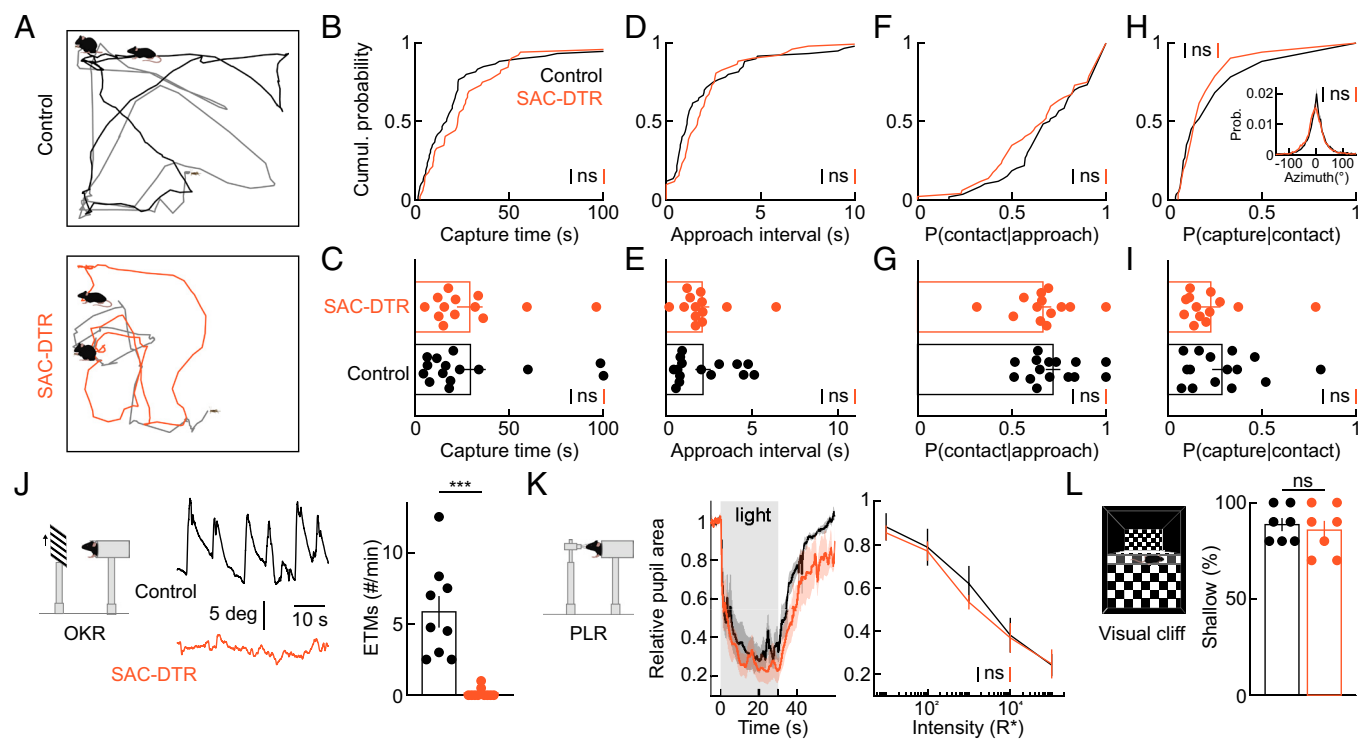


**Fig. 4.** Impact of eliminating retinal direction selectivity on visual behaviors. (A) Traces of representative hunting trials of control (black) and SAC-DTR mice (orange) injected with diphtheria toxin. (B and C) Summary data comparing capture times of control and SAC-DTR mice across all trials (B, control n = 60 trials, SAC-DTR n = 52 trials) or after the four trials of each mouse (C, control n = 15 mice, SAC-DTR n = 13 mice). (D and E) analogous to (B and C) for approach intervals. (F and G) analogous to (B and C) for the probability of converting approaches into contacts. (H and I) analogous to (B and C) for the probability of converting contacts into captures. The Inset in H shows the distribution of the cricket in azimuth within the head-centric visual field of mice during approach and contact. (J) Left: Representative eye tracking traces recorded from head-fixed awake mice during presentation of a vertically drifting grating stimulus. Right: Summary data of eye tracking movements per minute in control (black, n = 9 mice) and SAC-DTR mice (orange, n = 10 mice) injected with diphtheria toxin. (K) Left: Response traces (mean  $\pm$  SEM) of pupil constriction to a light step in control and SAC-DTR mice injected with diphtheria toxin. Right: Summary data of the intensity responses functions of the pupillary light responses in control (n = 4 mice) and SAC-DTR mice (n = 4 mice) injected with diphtheria toxin. (L) Summary data comparing the performance of control (n = 7 mice) and SAC-DTR mice (n = 7 mice) injected with diphtheria toxin in a visual cliff test. Throughout this figure, ns indicates  $P > 0.05$  and \*\*\* $P < 0.001$ .

system (i.e., the medial and dorsal terminal nuclei and the nucleus of the optic tract). This did not affect the hunting performance of mice (*SI Appendix*, Fig. S2), indicating that predation is independent of direction-selective signals to the SC, which orients the gaze, and the accessory optic system, which stabilizes it (11, 37).

## Discussion

Our study supports five main conclusions: 1) direction-selective responses of NF cells in the SC are independent of stimulus-edge effects; 2) NF cells receive direct synaptic input from ooDSGCs; 3) SC neurons, including NF cells, inherit direction selectivity from the retina; 4) NF cells guide predation; and 5) NF cells guide predation independent of their direction selectivity.

We recorded SC neurons in awake head-fixed mice and found that direction-selective cells have smaller receptive fields than their non-direction-selective neighbors (Fig. 1). NF cells in the SC were first identified by their narrow dendrite arbors spanning the depth of the retinorecipient superficial SC (i.e., narrow-field vertical cells) (38, 39). This morphologic identification was subsequently formalized by quantitative clustering (14). In addition, NF cells were shown to differ from other SC neurons in their intrinsic excitability and axonal projection patterns, and are selectively labeled in Grp-Cre mice (7, 14). The small receptive fields of NF cells arise from the interaction of their narrow dendrite arbors with precise retinotopically organized ganglion cell axons in the SC (14, 40). Early recordings showed that many NF cells (~50%) are direction-selective (7, 14). However, a

recent study revealed that orientation and direction-selective responses can be artificially induced in SC neurons with receptive fields near stimulus edges (16). To avoid this confound, we presented visual stimuli in a dome encompassing a large area of the mouse's visual field (180 deg azimuth  $\times$  120 deg elevation) and restricted our analyses to neurons with receptive fields  $>20$  deg from the edge. In these settings, we found that many SC neurons with receptive fields  $<300$  deg $^2$ , a size characteristic of NF cells (7, 14), are direction-selective. Together with the prior work (7, 14), this suggests that many NF cells are direction-selective, independent of stimulus-edge effects.

The origins of direction selectivity in the SC have been debated (17, 18), and the source of direction selectivity in NF cells was unknown. Before vision, the developing retina generates waves of spontaneous activity that propagate through the early visual system, shaping circuit development (41). In their later stages, waves spread preferentially in the temporal-to-nasal direction of the retina, foreshadowing activity patterns generated by optic flow when mice move forward (18, 42, 43). Recent work revealed that retinal waves and their propagation bias regulate the development of direction selectivity in the retina and SC (18, 43). Earlier, Shi et al. (17) concluded that direction selectivity in the SC is inherited from the retina. However, this conclusion was based on a manipulation (i.e., blocking GABA release from starburst amacrine cells) now known to abolish the propagation bias of retinal waves, raising concerns that the observed effects reflected changes in circuit development. Indeed, Ge et al. (18) reported that acute intraocular injections of a GABA<sub>A</sub> receptor blocker, expected to eliminate retinal direction selectivity, did not

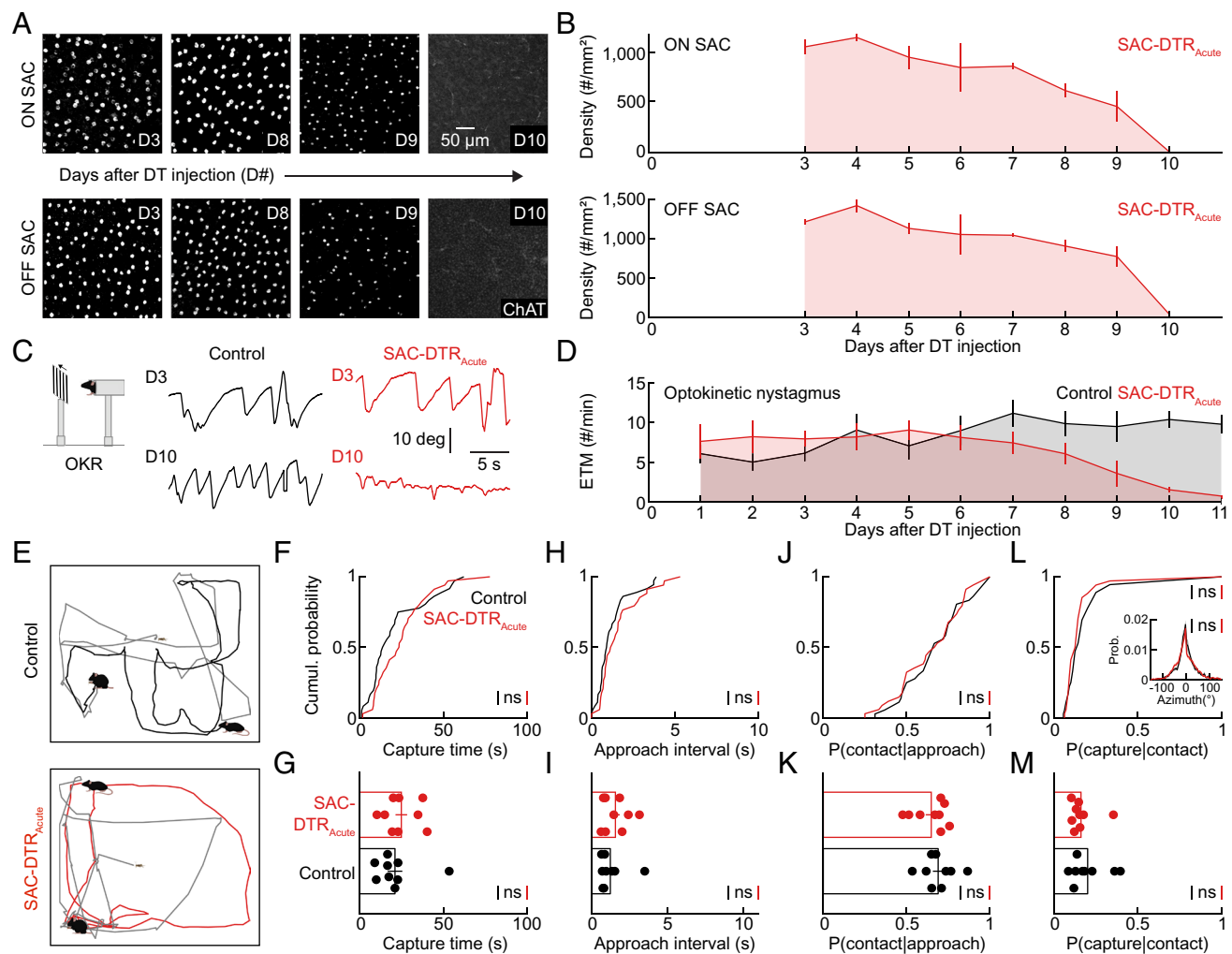


**Fig. 5.** Acute elimination of retinal direction selectivity does not disrupt predation. (A) Representative confocal images of retinal flat mounts stained for ChAT showing the time course of starburst amacrine cell removal in the ganglion cell (ON SAC) and inner nuclear layers (OFF SAC) after diphtheria toxin injection. (B) Summary data of the decline in starburst amacrine cell density ( $n = 3$  to 4 mice per time point). (C and D) Representative traces (C) and summary data (D) of the optokinetic response in control and SAC-DTR mice as a function of time after binocular diphtheria toxin injections at day 0 ( $n = 3$  to 5 mice per time point). (E) Traces of representative hunting trials of control (black) and SAC-DTR mice (red) injected with diphtheria toxin. (F and G) Summary data comparing capture times of control and SAC-DTR mice across all trials (F, control  $n = 36$  trials, SAC-DTR  $n = 34$  trials) or after the three to four trials of each mouse (G, control  $n = 9$  mice, SAC-DTR  $n = 9$  mice). (H and I) Analogous to (F and G) for approach intervals. (J and K) Analogous to (F and G) for the probability of converting approaches into contacts. (L and M) Analogous to (F and G) for the probability of converting contacts into captures. The Inset in L shows the distribution of the cricket in azimuth within the head-centric visual field of mice during approach and contact.

disrupt direction-selective responses in the SC, suggesting the latter are at least partially independent of the former. However, suppression of retinal direction selectivity was not confirmed, and the injections and recordings were performed around eye-opening when circuits were still immature (18). Finally, both Shi et al. (17) and Ge et al. (18) focused analyses on the most superficial layers of the SC, where direction-selective responses are restricted mainly to Clbn4-positive interneurons (15). We removed starburst amacrine cells from the retina of adult mice and confirmed that this eliminated direction-selective responses in ooDSGCs (Fig. 3) and the optokinetic reflex (Figs. 4 and 5). We found that this manipulation abolished direction-selective responses throughout the SC, including in neurons with narrow receptive fields (Fig. 3 and *SI Appendix*, Fig. S1). Using retrograde rabies virus tracing, we also showed that NF cells receive synaptic input from ooDSGCs (Fig. 2), consistent with results from disynaptic and anterograde tracing (24, 44). Together, these findings indicate that neurons in the SC, including NF cells, inherit direction-selective responses from ooDSGCs in the retina.

NF cells are critical for predation (Fig. 1) (7). They contribute to prey detection and mediate pursuit and capture (Fig. 1) (7). Direction-selective signals of NF cells and similar cells in the SC and its orthologs across the animal kingdom are thought to guide orientating behaviors, including predatory pursuits (6–10, 14, 45, 46). However, because most perturbations either silence all responses or remove neurons, causal links between specific feature computations and visual behaviors remain untested. Since NF cells inherit their direction selectivity from the retina, we could selectively eliminate this feature computation without silencing NF cells. Surprisingly, this revealed that NF cells guide predation independent of their direction selectivity, even when direction-selective responses are eliminated after mice learn to hunt (Figs. 4 and 5). NF cells have complex feature preferences besides direction selectivity, preferring negative over positive contrast and responding robustly to motion in a specific range of speeds and a narrow region of visual space. These properties match features of the cricket in the retinal image during predation (negative contrast, size: ~6 deg, speed: ~19 deg/s) (34) and the parameters

of artificial visual stimuli eliciting approaches (negative contrast, optimal size: ~5 deg, optimal speed: <50 deg/s) (3). These preferences likely arise, in part, from the input of non-ooDSGCs to NF cells, an exciting area for future exploration. Our study highlights the importance of feature-selective circuit manipulations for linking neural computation to behavior, a central goal of neuroethology.

## Materials and Methods

**Animals.** In this study, we used the following mouse lines: Grp-Cre (i.e., Grp-KH288-Cre)(47), ChAT-Cre (strain #: 006410)(48), floxed diphtheria toxin receptor (HiDTR, The Jackson Laboratory, strain #007900)(49), and DRD4-EGFP (29). In the retina, ChAT-Cre drives recombination selectively in starburst amacrine cells; we refer to crosses of ChAT-Cre and HiDTR mice, as SAC-DTR. All mice were backcrossed onto a C57BL/6J (The Jackson Laboratory, strain #: 000664) background for at least five generations. Experiments were performed on adult mice (2 to 4 mo old) of both sexes housed on a 12-h light/12-h dark cycle. We observed no sex-specific differences in our results and, therefore, combined data from male and female mice. The procedures in this study were approved by the Animal Studies Committee of Washington University School of Medicine (Protocol # 23-0116) and performed in accordance with the NIH Guide for the Care and Use of Laboratory Animals.

**Viruses.** We injected the adeno-associated virus AAV5-EF1 $\alpha$ -FLEX-taCasp3 (Addgene #: 45580-AAV5) (22) into Grp-Cre mice (i.e., NF-Casp3) to remove narrow-field (NF) neurons in the superior colliculus (SC). As controls, Grp-Cre mice were injected with AAV-hSyn-FLEX-jGCaMP6s (Addgene #: 100845-AAV9) (23). To silence neurons in the accessory optic system, we injected the respective brain areas with AAV5-hSyn-hM4D(Gi)-mCherry (i.e., AAV-DREADD), Addgene #: 50475-AAV5. We used monosynaptic rabies virus tracing to identify retinal ganglion cells providing input to NF neurons in the SC (25). We injected AAV8-hSyn-FLEX-TVA-P2A-eGFP-2A-oG (Salk Institute Vector core #: 85225), followed 3 to 4 wk later by EnVA- $\Delta$ G-mCherry (i.e., a pseudotyped and G-deleted rabies virus; Salk Institute Vector core #: 32636) (26).

**Surgical Procedures.** For all surgical procedures, mice were anesthetized by intraperitoneal (i.p.) injection of a cocktail (0.1 mL/20 g body weight) of ketamine HCl (87 mg/kg) and xylazine (13 mg/kg). We administered meloxicam (5 mg/kg) postoperatively by subcutaneous injection at 0, 24, and 48 h. For craniotomies and headplate attachments, the scalp was sanitized with betadine solution and 70% ethanol before incisions were made to expose the skull. Mice were mounted in a stereotaxic frame, and 100 to 200 nL of virus was delivered to specific brain areas through appropriately placed craniotomies via a Nanoject III system (Drummond Scientific). In this study, we targeted bilateral injections to the SC ( $\pm$ 0.75 to 1 mm M/L; -3.25 to -4 mm A/P; 1.2 to 1.7 mm depth), the medial terminal nucleus (MTN:  $\pm$ 1 mm M/L; -3.26 mm A/P; 4.31 mm depth), the dorsal terminal nucleus (DTN:  $\pm$ 1.80 to 1.89 mm M/L; -3.51 mm A/P; 2.66 to 2.78 mm depth), and the nucleus of the optic tract (NOT:  $\pm$ 0.87 to 0.9 mm M/L; -2.9 mm A/P; 2.02 to 2.11 mm depth) (50). After injections, the skin over the surgical sites was closed with staples and allowed to heal for 7 to 10 d before removing the staples. To install headplates, the periosteum was removed from the exposed skull with a scalpel and application of 3% H<sub>2</sub>O<sub>2</sub> solution. After washing with PBS, the skull was thoroughly dried and abraded with a scalpel to improve adhesion. Custom titanium headplates (eMachineShop.com) were fixed to the mouse skull using tissue adhesive (Vetbond, 3M) and dental cement (C&B Metabond, Parkell). Before headplates were installed for electrophysiology, the positions of subsequent craniotomies were marked. We allowed mice to recover for at least three days before acclimating to head fixation in the behavioral or *in vivo* electrophysiology training apparatus. We increased the acclimation time gradually each day until the expected experiment duration was reached. Diphtheria toxin (DT: 1.6 ng in 2  $\mu$ L PBS) was injected intravitreally via a Nanoject II system (Drummond) into both eyes of SAC-DTR and control mice.

**Tissue Preparation.** Mice were deeply anesthetized with CO<sub>2</sub> and killed by cervical dislocation. For immunohistochemistry, brains were removed and fixed in 4% paraformaldehyde overnight. Retinas were isolated after enucleation in oxygenated mACSF<sub>HEPES</sub> containing (in mM) 119 NaCl, 2.5 KCl, 1 NaH<sub>2</sub>PO<sub>4</sub>, 2.5 CaCl<sub>2</sub>, 1.3 MgCl<sub>2</sub>, 20 HEPES, and 11 glucose (pH adjusted to 7.37 with NaOH). The isolated

retinas were flat-mounted on black membrane disks (Millipore). Alternatively, retinas were fixed in the eyecup with 4% paraformaldehyde for 20 min. For retinal electrophysiology experiments, mice were dark-adapted for >1.5 h, enucleated under dim-red light, and retinas isolated under infrared illumination (>900 nm) in oxygenated mACSF<sub>NaHCO<sub>3</sub></sub> containing (in mM) 125 NaCl, 2.5 KCl, 1 MgCl<sub>2</sub>, 1.25 NaH<sub>2</sub>PO<sub>4</sub>, 2 CaCl<sub>2</sub>, 20 glucose, 26 NaHCO<sub>3</sub>, and 0.5 L-glutamine equilibrated with 95% O<sub>2</sub>/5% CO<sub>2</sub>. Isolated retinas were flat-mounted with the ganglion cells facing up on transparent membrane discs (Anodisc, Whatman).

**Immunohistochemistry.** We cut vibratome slices of brains (thickness: 100  $\mu$ m) targeting regions of interest (SC and AOS). Retinal eye cups were embedded in 4% low-melt agarose to cut vibratome slices (thickness: 60  $\mu$ m). Retina and brain slices were blocked in 10% normal donkey serum (NDS) in PBS for 2 h, incubated for 2 d in primary antibodies at 4 °C, washed three times in PBS for 30 min, and incubated in secondary antibodies for 2 h. Flat-mounted retinas were cryoprotected (1 h 10% sucrose in PBS, 1 h 20% sucrose in PBS, and overnight 30% sucrose in PBS at 4 °C) and then frozen and thawed three times. Flat-mounted retinas were then blocked with 5% NDS in PBS for 2 h, incubated in primary antibodies for 5 d at 4 °C, washed three times in PBS for 1 h, and incubated in secondary antibodies for 2 d. We used the following primary antibodies: goat anti-ChAT (Abcam, RRID:AB\_2079595), rabbit anti-CART (Phoenix Peptide, RRID:AB\_948257), and rabbit anti-DsRed (BD Biosciences, RRID:AB\_394264). Primary antibodies were visualized with secondary antibodies conjugated to Alexa 488, 568, or 633 (ThermoFisher), and cell nuclei were labeled with DAPI.

**Confocal Imaging and Analysis.** Confocal images were acquired on an Fv1000 laser scanning microscope (LSM, Olympus) using either a 60 $\times$  1.35 NA oil immersion objective or a 20 $\times$  0.85 NA oil objective. Voxel sizes varied from 0.103  $\mu$ m (x/y)–0.3  $\mu$ m (z) to 0.309  $\mu$ m (x/y)–1  $\mu$ m (z). We counted starburst amacrine cells in SAC-DTR and control mice using the Cell Counter feature of Fiji on retinal flat mounts stained for ChAT (51). We identified CART-positive retrogradely labeled (mCherry-positive) cells in retinal flat mounts by eye.

**Two-Photon-Guided Patch-Clamp Recordings, Visual Stimulation, and Analysis.** We obtained whole-cell patch-clamp recordings from ganglion cells in the dorsal halves of dark-adapted (>1.5 h), flat-mounted retinas. Throughout the recordings, retinas were perfused (~3 mL/min) with warm (~32 °C) mACSF<sub>NaHCO<sub>3</sub></sub>. We targeted fluorescent ganglion cells in DRD4-EGFP mice (i.e., ON-OFF DS RGCS) and after retrograde tracing of retinal inputs to the SC in Grp-Cre mice under two-photon guidance on an Fv1000 MPE system (Olympus) with a Mai Tai DeepSee laser (Spectra-Physics). Patch pipettes with resistances of 4 to 6 M $\Omega$  were pulled from borosilicate glass using a P97 puller (Sutter Instruments). The intracellular solution for current-clamp recordings contained (in mM) 125 K-gluconate, 10 NaCl, 1 MgCl<sub>2</sub>, 10 EGTA, 5 HEPES, 5 ATP-Na<sub>2</sub>, and 0.1 GTP-Na (pH adjusted to 7.2 with KOH).

We presented visual stimuli on an organic light-emitting display (eMagin) and projected them onto the photoreceptor side of the dorsal retina via the substage condenser. We recorded spike responses to square-wave gratings (wavelength: 200  $\mu$ m) drifting in eight equally spaced pseudorandomly ordered directions (temporal frequency: 1 to 2 Hz). To measure direction preferences, the average firing rates of a neuron to each drift direction were computed and the average firing rate in response to interleaved uniform gray stimuli of the same mean luminance (~5,000 rhodopsin isomerizations/rod/s or R\*) subtracted. A direction selectivity index (DSI) and the preferred stimulus direction were then calculated based on the circular variance of the response R as follows:

$$\text{DSI} = \left| \frac{\sum R(\theta)e^{i\theta}}{\sum R(\theta)} \right|,$$

where  $\theta$  is the stimulus direction. The DSI is given by the absolute amplitude of this relationship, whereas the preferred direction is defined by its complex phase (52).

**In Vivo Electrophysiology, Visual Stimulation, and Analysis.** We allowed mice to recover for three to five days after headplate installation before acclimating them to a training setup. They were head-fixed and free to run on a cylindrical treadmill while being shown white noise stimuli to simulate recording conditions. Approximately 24 h before recordings, we drilled small craniotomies at the marked SC coordinates, removed the underlying dura mater, washed the region with PBS, and covered the craniotomies with Kwik-Cast silicone sealant (WPI).

On the day of recording, the Kwik-Cast was removed, and the headplate chamber above the craniotomy was filled with sterile PBS. 32-channel silicon probes (A1x32-Poly2-5 mm-50 s-177 or A1x32-Poly3-5 mm-25 s-177, NeuroNexus) were slowly (~1  $\mu$ m/s) inserted into the brain. Before insertion, probes were coated with Dil to mark the recording site. Neural signals were digitized at 30 kHz (Smartbox, NeuroNexus). We sorted spike trains offline with Kilosort3 (53) and analyzed them using custom MATLAB (The Mathworks) scripts.

We presented visual stimuli on a custom dome covering 180 deg azimuth  $\times$  120 deg elevation of the mouse visual field. The dome was constructed using an 18-inch diameter transparent poly-carbonate sphere (California Quality Plastics) and was treated with a specialized UV-reflective paint (Twilight Laboratory), formulated to consistently reflect spectral ranges from 350 to 600 nm while mitigating internal reflections (54). Mice were secured at the head on a cylindrical treadmill situated at the dome's center, which allowed them to run freely. This positioning also placed the mice's eyes at the core of the spherical coordinate system formed by the dome. The movement of the mice running on the treadmill was captured by a rotary encoder (Yumo) and subsequently recorded via an Arduino board.

Stimuli were projected onto the surface of the dome using an E4500 MKII PLUS II projector (EKB Technologies), which was illuminated by LEDs emitting light at 385 nm, 460 nm, and 520 nm to align with the mouse photoreceptor complement. These stimuli were reflected off a spherical mirror (Grainger). Stimuli were presented via PsychoPy (55) and adjusted to fit the dome's dimensions through a customized version of the meshmapper utility, accessible at <http://paulbourke.net/dome/meshmapper/>. Fine-tuning of the warp calibration was performed to amend spatial distortions across the dome, viewed from the mouse's visual field perspective. To ensure linearity of illuminance values, the projector underwent gamma correction and calibration. Additionally, ND filters (ThorLabs) were positioned in the projector's light path to regulate the dome's illuminance.

To identify visually responsive units within the superficial SC, we first displayed 60 s of an inverting checkerboard stimulus (1 Hz, 12.5 deg  $\times$  12.5 deg check size, 100% contrast). The border between the superficial and intermediate/deep SC was calculated using current source density analysis and estimated from the inflection depth at the current source-sink transition (56). The probe position within the superficial superior colliculus was confirmed histologically after each experiment. To assess receptive field sizes, we presented a flashing spot (1 Hz, 10 deg, 100% contrast, ten repeats) at each coordinate across the entire azimuth and elevation of the dome. Direction-selective units were identified with a field of drifting spots (4-deg spots, 100% contrast) moving in eight directions (0, 45, 90, 135, 180, 225, 270, and 315 deg) at varying speeds (5, 10, 20, 40, and 80 deg/s). The field of spots drifted with a given direction and speed for 2 s, then paused for 1 s before drifting with a new direction and speed. Drift directions and speeds were presented in pseudorandom orders.

The DSI of responses was calculated by the formula in the section on two-photon-guided patch clamp recordings, visual stimulation, and analysis. An orientation selectivity index (OSI) was calculated from the circular variance of the response ( $R$ ) as follows:

$$\text{OSI} = \left| \frac{\sum R(\theta) e^{2i\theta}}{\sum R(\theta)} \right|,$$

where  $\theta$  is the stimulus direction. The OSI is given by the absolute amplitude of this relationship, whereas the preferred orientation is defined by its complex phase (52). A speed preference index (SPI) was defined as

$$\text{SPI} = \frac{R_{\text{Fast}} - R_{\text{Slow}}}{R_{\text{Fast}} + R_{\text{Slow}}},$$

where  $R_{\text{Fast}}$  and  $R_{\text{Slow}}$  denote the average responses to motion in the preferred direction at 20 and 40 deg/s vs. 5 and 10 deg/s, respectively. A contrast preference index (CPI) was calculated as

$$\text{CPI} = \frac{RF_{\text{ON}} - RF_{\text{OFF}}}{RF_{\text{ON}} + RF_{\text{OFF}}},$$

where  $RF_{\text{ON}}$  and  $RF_{\text{OFF}}$  refer to the ON and OFF receptive field peaks, respectively.

**Predation.** We tested insect predation with a protocol similar to those previously described (33, 34). Two days before training began, mice were individually housed, acclimated to handling, and two or three crickets were introduced to each cage in addition to food pellets. Food was restricted 16 to 20 h before training (i.e., food pellets were removed from the cages, and each mouse was given two or three crickets). On the first training day, mice were introduced to the behavioral arena (width: 45 cm, length: 38 cm, height: 30 cm, with padded flooring) and given 3 min to acclimate. A cricket was then placed in the arena, and mice were given up to 5 min to capture it. After 5 min or after the successful capture of the cricket, the arena was cleaned, and a new cricket introduced, until each mouse had the opportunity to capture three crickets. The interactions between mice and crickets were recorded with an overhead camera (C310, Logitech). After three trials, mice were returned to their home cages and given access to food pellets for 4 to 6 h, before food pellets were removed again 16 to 20 h before the next training session. Mice were trained for 5 d when their hunting performance had plateaued, and their performance tested on the sixth day.

Mice expressing AAV-DREADDI or control viruses received PBS i.p. injections on days four, five, and six. They received CNO i.p. (1 mg/kg) on day six. Hunting performance was compared between CNO- and PBS-injected trials spaced at least 4 h apart on day six to minimize variability.

In SAC-DTR mice, a single intraocular DT injection elicited synchronous starburst amacrine cell death after 10 d (Fig. 5). We took advantage of this timing to ablate starburst amacrine cells before training began (i.e., DT injection 2 wk before training began) or as training concluded before testing began. In the latter experiment, training began 4 d after the DT injection, with testing on day 10. Mice were killed immediately after testing to confirm starburst amacrine cell removal.

Overhead videos were analyzed in DeepLabCut (57, 58) to track the positions of the cricket and the mouse's ears, nose, and tail base. Custom software (OpenCV, Python) was used to extrapolate the mouse's position relative to the cricket, as previously described (34). For each trial, we calculated the overall time to capture, the number of approaches made by the mouse, and the interval between approaches, a measure of prey detection. Approaches were defined as periods when the mouse was running at speeds  $>10$  cm/s and decreased the distance between the mouse and the cricket by  $>7$  cm/s. Approaches concluded when these criteria were no longer met or when the mouse contacted (distance:  $<4$  cm) the cricket. We calculated the conditional probabilities of converting approaches to contacts and contacts to captures to quantify the efficacy of the visual pursuit and capture, respectively (34). We evaluated prey detection by the interval between the end of an approach or contact and the start of the following approach.

**Pupillary Light Responses.** Pupil responses were recorded and tracked with infrared illumination of the left eye of head-fixed awake mice with an ETL-200 eye-tracking system (ISCAN) (34). At the same time, we presented stimuli were presented to the mouse's right eye via an Arduino-controlled 525 nm LED (Thorlabs), adjusting the stimulus intensity through a set of ND filters (Thorlabs). To assess the PLR, we presented illuminance steps from  $10^0$  to  $10^5$  R\* in  $10^{0.5}$  increments. Steps were presented from darkness for 30 s, followed by 30 s postillumination recovery to baseline. Stimuli were separated by a minimum of 2 min in darkness. We normalized pupil constriction to the area of the pupil when fully adapted to darkness. The relative area of the pupil for each light level was then determined by averaging the pupil size over a 5-s period at the point of greatest constriction. To calculate the EC<sub>50</sub> values, which indicate the light intensity at which half-maximal pupil constriction occurs, we applied a Hill equation model to the collected data from each subject.

**Optokinetic Responses.** For OKR experiments, we presented visual stimuli using the Cogent Graphics toolbox (John Romaya, Laboratory of Neurobiology at the Wellcome Department of Imaging Neuroscience, University College London) in MATLAB (The MathWorks). Eye movements were recorded and tracked with infrared illumination of the left eye using the ETL-200 eye-tracking system (ISCAN). We tested the optokinetic reflex with square-wave gratings (0.05 cycles/deg) at varying Michelson contrasts (10, 20, 50, and 100%) moving at 10 deg/s in the temporal-nasal and/or upward direction on a monitor placed 11 cm from the mouse's left eye (angle: 45°). Each stimulus presentation consisted of 10 s of a uniform gray screen, 60 s of a drifting grating, and another 10 s of a gray screen. Stimuli were repeated twice for each mouse. We measured eye-tracking movements (ETMs) as the number of saccade-like eye movements following a slow tracking motion (59).

**Visual Cliff.** We assessed depth perception with a visual cliff test (60). Mice were placed on a ridge (width: 3.8 cm; height: 3.4 cm) running across the center of a transparent 56 cm (width) by 41 cm (depth) platform. On one side of the ridge, a checkered pattern was immediately below the platform (i.e., the shallow side). On the other side, an identical checkered pattern was 61 cm below the platform (i.e., the cliff side). Mice were filmed on an overhead camera (C310, Logitech), and the fraction of shallow-side choices in ten trials was measured.

**Statistics.** Throughout our study, we evaluated the statistical significance of differences between experimental groups (e.g., capture times in NF-Casp3 vs. control mice) by Mann–Whitney *U* tests. We compared the intensity response functions of pupillary light responses in SAC-DTR vs. control mice (Fig. 4*K*) by bootstrapping.

1. K.T. Sillar, L.D. Picton, W.J. Heitler, *The Neuroethology of Predation and Escape* (John Wiley & Sons, 2016).
2. J.P. Ewert, Neural correlates of key stimulus and releasing mechanism: A case study and two concepts. *Trends Neurosci.* **20**, 332–339 (1997).
3. N.M. Procacci *et al.*, Context-dependent modulation of natural approach behaviour in mice. *Proc. Biol. Sci.* **287**, 20201189 (2020).
4. V. Nityananda, J. O’Keeffe, D. Umeton, A. Simmons, J. C. A. Read, Second-order cues to figure motion enable object detection during prey capture by praying mantises. *Proc. Natl. Acad. Sci. U.S.A.* **116**, 27018–27027 (2019).
5. F.R. Prete, Stimulus configuration and location in the visual field affect appetitive responses by the praying mantis, *Sphodromantis lineola* (Burr.). *Vis. Neurosci.* **10**, 997–1005 (1993).
6. I.H. Bianco, F. Engert, Visuomotor transformations underlying hunting behavior in zebrafish. *Curr. Biol.* **25**, 831–846 (2015).
7. J.L. Hoy, H.I. Bishop, C.M. Niell, Defined cell types in superior colliculus make distinct contributions to prey capture behavior in the mouse. *Curr. Biol.* **29**, 4130–4138.e5 (2019).
8. F. Scarano, D. Tomsic, J. Szarker, Direction selective neurons responsive to horizontal motion in a crab reflect an adaptation to prevailing movements in flat environments. *J. Neurosci.* **40**, 5561–5571 (2020).
9. B.J. E. Evans, D.C. O’Carroll, J.M. Fabian, S.D. Wiederman, Dragonfly neurons selectively attend to targets within natural scenes. *Front. Cell. Neurosci.* **16**, 857071 (2022).
10. D. Förster *et al.*, Retinotectal circuitry of larval zebrafish is adapted to detection and pursuit of prey. *Elife* **9**, e58596 (2020).
11. M.A. Basso, M.E. Bickford, J. Cang, Unraveling circuits of visual perception and cognition through the superior colliculus. *Neuron* **109**, 918–937 (2021).
12. J.R. Sanes, S.L. Zipursky, Design principles of insect and vertebrate visual systems. *Neuron* **66**, 15–36 (2010).
13. D.O’Carroll, Feature-detecting neurons in dragonflies. *Nature* **362**, 541–543 (1993).
14. S.D. Gale, G.J. Murphy, Distinct representation and distribution of visual information by specific cell types in mouse superficial superior colliculus. *J. Neurosci.* **34**, 13458–13471 (2014).
15. Y. Liu *et al.*, Mapping visual functions onto molecular cell types in the mouse superior colliculus. *Neuron* **111**, 1876–1886.e5 (2023), 10.1016/j.neuron.2023.03.036.
16. Y. Liang, R. Lu, K. Borges, N.J. Ji, Stimulus edges induce orientation tuning in superior colliculus. *Nat. Commun.* **14**, 4756 (2023).
17. X. Shi *et al.*, Retinal origin of direction selectivity in the superior colliculus. *Nat. Neurosci.* **20**, 550–558 (2017).
18. X. Ge *et al.*, Retinal waves prime visual motion detection by simulating future optic flow. *Science* **373**, eabd0830 (2021).
19. E. L. Savier, H. Chen, J. Cang, Effects of locomotion on visual responses in the mouse superior colliculus. *J. Neurosci.* **39**, 9360–9368 (2019).
20. S. Ito, D.A. Feldheim, A.M. Litke, Segregation of visual response properties in the mouse superior colliculus and their modulation during locomotion. *J. Neurosci.* **37**, 8428–8443 (2017), 10.1523/JNEUROSCI.3689-16.2017.
21. H. Chen, E. L. Savier, V.J. DePiero, J. Cang, Lack of evidence for stereotypical direction columns in the mouse superior colliculus. *J. Neurosci.* **41**, 461–473 (2021).
22. C. F. Yang *et al.*, Sexually dimorphic neurons in the ventromedial hypothalamus govern mating in both sexes and aggression in males. *Cell* **153**, 896–909 (2013).
23. T.-W. Chen *et al.*, Ultrasensitive fluorescent proteins for imaging neuronal activity. *Nature* **499**, 295–300 (2013).
24. K. Reinhard *et al.*, A projection specific logic to sampling visual inputs in mouse superior colliculus. *Elife* **8**, e50697 (2019).
25. E.M. Callaway, L. Luo, Monosynaptic circuit tracing with glycoprotein-deleted rabies viruses. *J. Neurosci.* **35**, 8979–8985 (2015).
26. E.J. Kim, M.W. Jacobs, T. Ito-Cole, E.M. Callaway, Improved monosynaptic neural circuit tracing using engineered rabies virus glycoproteins. *Cell Rep.* **15**, 692–699 (2016).
27. J.N. Kay *et al.*, Retinal ganglion cells with distinct directional preferences differ in molecular identity, structure, and central projections. *J. Neurosci.* **31**, 7753–7762 (2011).
28. D. Hillier *et al.*, Causal evidence for retina-dependent and -independent visual motion computations in mouse cortex. *Nat. Neurosci.* **20**, 960–968 (2017), 10.1038/nn.4566.
29. A.D. Huberman *et al.*, Genetic identification of an On-Off direction-selective retinal ganglion cell subtype reveals a layer-specific subcortical map of posterior motion. *Neuron* **62**, 327–334 (2009).
30. M. Rivlin-Etzion *et al.*, Transgenic mice reveal unexpected diversity of on-off direction-selective retinal ganglion cell subtypes and brain structures involved in motion processing. *J. Neurosci.* **31**, 8760–8769 (2011).
31. J.H. Marshel, A.P. Kaye, I. Nauhaus, E.M. Callaway, Anterior-posterior direction opponency in the superficial mouse lateral geniculate nucleus. *Neuron* **76**, 713–720 (2012).
32. L. Liang *et al.*, A fine-scale functional logic to convergence from retina to thalamus. *Cell* **173**, 1343–1355.e24 (2018).
33. J.L. Hoy, I. Pavorska, M. Wehr, C.M. Niell, Vision drives accurate approach behavior during prey capture in laboratory mice. *Curr. Biol.* **26**, 3046–3052 (2016).
34. K.P. Johnson *et al.*, Cell-type-specific binocular vision guides predation in mice. *Neuron* **109**, 1527–e4–1539.e4 (2021), 10.1016/j.neuron.2021.03.010.
35. K. Yoshida *et al.*, A key role of starburst amacrine cells in originating retinal directional selectivity and optokinetic eye movement. *Neuron* **30**, 771–780 (2001).
36. K. Yonehara *et al.*, Congenital nystagmus gene FRMD7 is necessary for establishing a neuronal circuit asymmetry for direction selectivity. *Neuron* **89**, 177–193 (2016).
37. J.I. Simpson, The accessory optic system. *Annu. Rev. Neurosci.* **7**, 13–41 (1984).
38. T.P. Langer, R.D. Lund, The upper layers of the superior colliculus of the rat: A Golgi study. *J. Comp. Neurol.* **158**, 418–435 (1974).
39. S.R.Y. Cajal, *Histology of the Nervous System of Man and Vertebrates* (Oxford University Press, 1995).
40. J. Sibille *et al.*, High-density electrode recordings reveal strong and specific connections between retinal ganglion cells and midbrain neurons. *Nat. Commun.* **13**, 1–18 (2022).
41. M.B. Feller, D. Kerschensteiner, “Chapter 16—Retinal waves and their role in visual system development” in *Synapse Development and Maturation*, J. Rubenstein *et al.*, Eds. (Academic Press, 2020), pp. 367–382.
42. B.K. Stafford, A. Sher, A.M. Litke, D.A. Feldheim, Spatial-temporal patterns of retinal waves underlying activity-dependent refinement of retinofugal projections. *Neuron* **64**, 200–212 (2009).
43. A. Tiriac, K. Bistrong, M.N. Pitcher, J.M. Tworog, M.B. Feller, The influence of spontaneous and visual activity on the development of direction selectivity maps in mouse retina. *Cell Rep.* **38**, 110225 (2022).
44. N.Y. Tsai *et al.*, Trans-Seq maps a selective mammalian retinotectal synapse instructed by Nephronectin. *Nat. Neurosci.* **25**, 659–674 (2022).
45. D. de Malmazet, N.K. Kühn, K. Farrow, Retinotopic separation of nasal and temporal motion selectivity in the mouse superior colliculus. *Curr. Biol.* **28**, 2961–2969.e4 (2018).
46. Z.M. Hafed, Superior colliculus: A vision for orienting. *Curr. Biol.* **28**, R1111–R1113 (2018).
47. C.R. Gerfen, R. Paletzki, N. Heintz, GENSAT BAC cre-recombinase driver lines to study the functional organization of cerebral cortical and basal ganglia circuits. *Neuron* **80**, 1368–1383 (2013).
48. J. Rossi *et al.*, Melanocortin-4 receptors expressed by cholinergic neurons regulate energy balance and glucose homeostasis. *Cell Metab.* **13**, 195–204 (2011).
49. T. Buch *et al.*, A Cre-inducible diphtheria toxin receptor mediates cell lineage ablation after toxin administration. *Nat. Methods* **2**, 419–426 (2005).
50. G. Paxinos, K.B.J. Franklin, *Paxinos and Franklin’s The Mouse Brain in Stereotaxic Coordinates* (Elsevier Science, 2019).
51. J. Schindelin *et al.*, Fiji: An open-source platform for biological-image analysis. *Nat. Methods* **9**, 676–682 (2012).
52. D.M. Piscopo, R.N. El-Danaf, A.D. Huberman, C.M. Niell, Diverse visual features encoded in mouse lateral geniculate nucleus. *J. Neurosci.* **33**, 4464–4456 (2013).
53. M. Pachitariu, S. Sridhar, C. Stringer, Solving the spike sorting problem with Kilosort. *bioRxiv* [Preprint] (2023). <https://doi.org/10.1101/2023.01.07.523036> (Accessed 30 September 2023).
54. D.J. Denman, J.H. Siegle, C. Koch, R.C. Reid, T.J. Blanche, Spatial organization of chromatic pathways in the mouse dorsal lateral geniculate nucleus. *J. Neurosci.* **37**, 1102–1116 (2017).
55. J.W. Peirce, PsychoPy—Psychophysics software in Python. *J. Neurosci. Methods* **162**, 8–13 (2007).
56. I. Stitt, E. Galindo-Leon, F. Pieper, G. Engler, A.K. Engel, Laminar profile of visual response properties in ferret superior colliculus. *J. Neurophysiol.* **110**, 1333–1345 (2013).
57. A. Mathis *et al.*, DeepLabCut: Markerless pose estimation of user-defined body parts with deep learning. *Nat. Neurosci.* **21**, 1281–1289 (2018), 10.1038/s41593-018-0209-y.
58. T. Nath *et al.*, Using DeepLabCut for 3D markerless pose estimation across species and behaviors. *Nat. Protoc.* **14**, 2152–2176 (2019).
59. H. Cahill, J. Nathans, The optokinetic reflex as a tool for quantitative analyses of nervous system function in mice: Application to genetic and drug-induced variation. *PLoS One* **3**, e2055 (2008).
60. T. Kim, N. Shen, J.-C. Hsiang, K.P. Johnson, D. Kerschensteiner, Dendritic and parallel processing of visual threats in the retina control defensive responses. *Sci. Adv.* **6**, eabc9920 (2020).
61. J. Krizan, M.J. Fitzpatrick, D. Kerschensteiner, Predation-without-direction-selectivity—code. GitHub. <https://github.com/kerschensteinerd/Predation-without-direction-selectivity—code>. Deposited 29 February 2024.

**Data, Materials, and Software Availability.** All study data are included in the article and/or *SI Appendix*. No new materials were generated for this study. The code for analyzing electrophysiological and behavioral data is available at <https://github.com/kerschensteinerd/Predation-without-direction-selectivity—code> (61).

**ACKNOWLEDGMENTS.** We are grateful to the members of the Kerschensteiner lab for helpful discussion throughout this project. This work was supported by funding from the NIH (EY013360 to J.K., EY034001 and EY026978 to D.K., and EY 027411 to D.K. and F.S.), the Hope Center for Neurological Disorders at Washington University (to D.K. and N.S.), the McDonnell Center for Systems Neuroscience at Washington University (to D.K.), the Grace Nelson Lacy Research Fund (to D.K.), and an unrestricted grant from Research to Prevent Blindness (to the Department of Ophthalmology and Visual Sciences).